

The LED calibration system of the SPHERE-2 detector



R.A. Antonov^a, E.A. Bonvech^a, D.V. Chernov^a, D.A. Podgrudkov^{a,b,*}, T.M. Roganova^a

^aSkobel'syn Institute for Nuclear Physics Lomonosov Moscow State University, Moscow, Russia

^bPhysics Department of Lomonosov Moscow State University, Moscow, Russia

ARTICLE INFO

Article history:

Received 24 July 2015

Revised 18 January 2016

Accepted 19 January 2016

Available online 23 January 2016

Keywords:

PMT

Calibration methods

Vavilov–Cherenkov radiation

Extensive air showers

ABSTRACT

An absolute calibration method for the PMT mosaic used in the SPHERE-2 experiment is presented. The method is based on the relative calibration of all PMTs in the mosaic to a single stable PMT, incorporated in it, during each measurement event and subsequent absolute calibration of that single PMT using a known stable light source. The results of the SPHERE-2 detector PMTs calibration are presented and are discussed.

© 2016 Elsevier B.V. All rights reserved.

1. Introduction

1.1. Reflected Vavilov–Cherenkov radiation method

SPHERE is a cosmic ray experiment based on the registration of reflected from the snow surface Vavilov–Cherenkov radiation generated by extensive air showers (EAS) [1]. The scientific goal of the SPHERE experiment is to study the primary cosmic ray spectrum and mass composition in the energy range $5 \cdot 10^{15}$ – $5 \cdot 10^{17}$ eV. The chosen optical method of EAS registration allows good primary energy measurements, but has low duty factor, thus the main goal in primary spectrum study is to achieve good estimation of the cosmic ray flux with low systematic uncertainties. The study of the primary mass composition is based on the event-by-event approach [2].

The idea of such an experiment was proposed by A.E. Chudakov in 1972 and was later described in [3]. In his idea a plane-mounted detector consisting of a pair of common photomultiplier tubes (PMT) and a pair of electro-optical converters (EOC) should have been observing the snow surface from a 10 km altitude. All four detectors were supposed to observe the same area and to have a viewing field of about 1.5–2 sr. The PMTs were planned as triggers for photocameras registering images from the EOCs. Images of the Vavilov–Cherenkov radiation spot on the snow should have provided detailed information on the EAS properties. Additionally the proposed detector had a sophisticated calibration system con-

sisting of a controlled flash-source aimed so as to produce spots of light in the field of view of the detector, e.g. artificial showers, which provided means for the relative and absolute calibration of the detector, snow surface properties measurements and atmosphere transparency control.

The proposed method of EAS registration features a quasi-continuous sensitive area unique for the ground based EAS detector arrays registering the lateral distribution of particles. This is possible due to the reflected Cherenkov light being collected from all of the visible to the detector surface rather than from separate points. Also the small size of the detector makes it easy to maintain and the compact configuration of the sensitive element (the PMT mosaic) allows a simple on-line relative and absolute calibration (which is described in this paper), means for detector state monitoring (the same as for fluorescent telescopes and imaging air Cherenkov telescopes). The airborne detector mount provides all means for atmospheric parameters control. Also, as a feature, the detector has a variable energy range with an almost constant counting rate. e.g. the change in the flight altitude results in the change of both the low and the high energy thresholds (both grow with altitude) in a way that the number of registered showers per hour is roughly constant for altitudes from 400 m up to 3 km.

In this paper only the calibration of the detector PMT mosaic is described and discussed. The energy calibration of the reconstructed events is described in [1,2].

1.2. SPHERE-2 detector

The SPHERE-2 apparatus was a balloon-borne detector lifted to about 400–900 m above the snow surface. The detector consisted of a control block, a 1.5 m diameter 0.94 m curvature radius

* Corresponding author. Tel.: +7 4959392437.

E-mail addresses: chr@dec1.sinp.msu.ru (D.V. Chernov), pyrocomp@gmail.com, d.a.podgrudkov@physics.msu.ru (D.A. Podgrudkov).

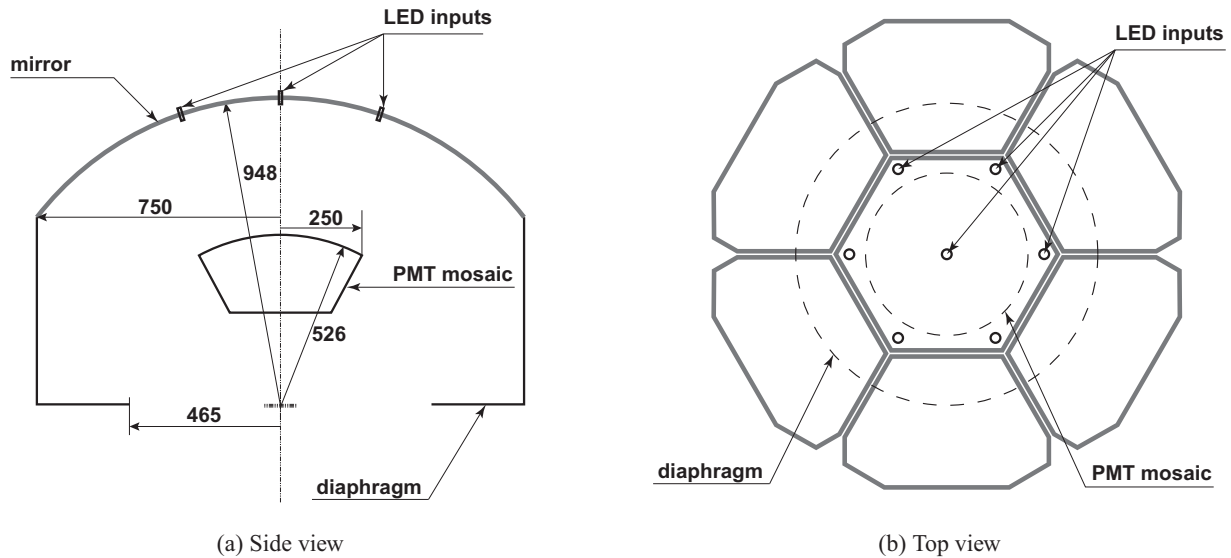


Fig. 1. Optical scheme of the SPHERE-2 detector.

spherical mirror with a photomultiplier tube mosaic near its focus (see Fig. 1) [4]. The mosaic in turn consisted of 109 PMTs (108 FEU-84-3 PMTs [5] and a Hamamatsu R3886 PMT [6]) arranged in a hexagonal grid.

The control block contained the batteries and the electronics, including the trigger system (TS), data acquisition system (DAQ), calibration system (CS) etc. [7]. The DAQ contained 10-bit flash analog-to-digital converters (FADC) with 80 MHz sampling frequency (e.g. 12.5 ns discretization). DAQ worked in a continuous mode first forking the signal from each PMT to TS and to a 6 μ s delay line. When the TS produced an ‘event’ signal the DAQ started recording 12.8 μ s of signal from the delay line (e.g. capturing $\sim 6 \mu$ s of the signal prior to the trigger) forming an ‘event’ frame. Each ‘event’ frame was paired by a ‘calibration’ frame (see below).

All measurements were performed on site at the Baikal Lake with a tethered balloon during the winter periods of 2010–2013.

1.3. The calibration system setup

The calibration system for SPHERE-2 consisted of a control board for 7 UV LEDs (FYL-5013VC1C [8]). The LED emission maximum was at 405 nm with a 15 nm width (manufacturer provided values). Each LED was controlled independently. The brightness of all LEDs was set to be more or less the same though for this method it is not relevant whether they have the same brightness or different. The only practical restriction was that if all of the LEDs flash together they should not saturate any PMTs in the mosaic or else this pulse will not be usable.

The light from the diodes was transferred to the mosaic via optical fibers. Each diode had its own outgoing fiber. The ends of the optical fibers were flat and coated in a matted material to produce a known (see Fig. 2) angular light distribution. On the mirror the ends of the fibers were fixed in the corners of the central hexagonal segment (LEDs number 2 to 7) and in its center (LED number 1). The fibers were fixed orthogonally to the mirror surface.

The LED control board 5.8 μ s after each TS signal produced a short (~ 200 ns) all-LED pulse. This pulse appeared at the end of each ‘event’ frame. Since all optical fibers were of the same length and the distances from their ends to the mosaic were relatively the same, this light pulse was simultaneous on all of the PMTs in the mosaic. So this pulse served for channel time shift detection and correction and for precise (less than 0.1 time bin size, e.g. about 1.5 ns) channel synchronization.

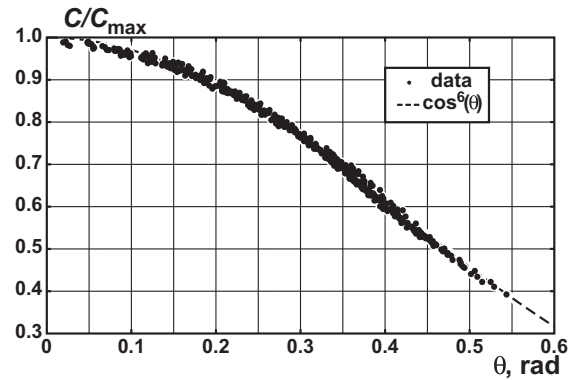


Fig. 2. Angular light intensity dependence for output from optical fiber 1. Dots represent data and line represents fit. The flattening at low angles is less than 1.5%.

Table 1

LED flashes pattern. ‘X’ indicates that a particular LED was on, empty cell indicates that it was off. Time slot is 375 ns long.

LED	Time slot														
	1	2	3	4	5	6	7	8	9	10	11	12	13	14	15
1	x	x	x	x	x	x	x								x
2	x	x	x	x	x	x	x								x
3	x	x	x	x	x	x							x		
4	x	x	x	x	x							x			
5	x	x	x	x							x				
6	x	x	x							x					
7	x	x							x						

18 μ s after the trigger the LED control board produced a series of pulses by individual LEDs and by their combinations. These pulses created a ‘calibration’ frame, used for a linearity check and relative calibration. The flashes pattern is shown in Table 1. The TS operated at a lower frequency than DAQ. So to avoid confusion with DAQ time bins the TS time quanta are called ‘time slots’. The time slot is 375 ns long, what corresponds to 30 time bins of signal measurement which is comparable with the Cherenkov light pulse duration from an EAS. This flash pattern allows to obtain a wide range of signals from each PMT for linearity check and gather sufficient data for stable calibration.

2. The method

The main idea of the presented calibration method is rather simple. After each TS signal the sensitive element of the detector is illuminated by a light source with a known angular distribution. The recorded signals are used to analyze the sensitivity of each pixel in comparison to the preselected one. This is similar to the methods used in Auger [9,10] and Telescope Array [11] for fluorescence telescopes or for cameras as in the planned CTA experiment [12] or in the on-going MAGIC experiment [13]. A similar method is proposed for JEM-EUSO experiment [14]. The main difference in the implementation of the described method in our case is that we did not try to achieve the spatial uniformity of the light field across the mosaic. In all of the above mentioned experiments a considerable effort is made to make the relative calibration light field pulse to be spatially uniform (as it greatly simplifies the analysis), but this is not necessary for the method itself. In our setup achieving a spatially uniform light field across the mosaic is a difficult task since the optical fibers outputs are close to the mosaic. Also a spatially uniform light field does not guarantee an equal number of photons reaching the PMTs' photocathodes due to reflections on the PMTs glass surfaces due to the relatively high incidence angles (up to 40°) for outer PMTs.

Since the FEU-84-3 PMTs are rather unstable under varying conditions, specifically the significant increase in sensitivity between the completely dark environment and with a starlight background (up to 25% increase in sensitivity), a stable Hamamatsu R3886 PMT was installed into the mosaic. A relative calibration procedure was done for each event to measure the sensitivity of each PMT relatively to the stable one. Later an absolute calibration procedure of the stable PMT was carried out.

The relative calibration was done by illuminating all of the PMTs by light-emitting diodes (LEDs) with a known light distribution over the mosaic. For this distribution the amount of photons reaching each PMT can be calculated. These numbers were then normalized to the number of photons in the selected stable PMT giving the ratios between signals in different PMTs. Then using signals from the calibration pulses a coefficient was selected for each PMT so that the ratio between the signal from this PMT and the signal in the stable PMT are equal to the calculated ratio.

3. Calibration system checks

3.1. Optical fiber check

To perform the relative calibration the distribution of light across the mosaic in the calibration pulse should be known. This distribution can be calculated for a known light distribution from a single fiber (a direct measurement was not possible due to technical reasons). So the fibers one by one were connected to a light source (ultra-bright 10 W white LED) on input and pointed to a white screen with a scale grid on it. The resulting light spot was photographed using a Practica DC34 camera (with a common CCD optical sensor). Another photo was taken under the same conditions without the spot to measure the background light distribution. The camera was then checked for linearity. The camera output was proven to be linear in our conditions, but showed noticeable non-linearity due to pixels over saturation by noise at higher light intensities. A picture of an evenly illuminated screen was taken in order to correct the camera zone sensitivity and possible screen unevenness. The pictures were converted to numerical arrays of light intensity. All components of the $2560 \times 1920 \times 3$ array were combined and averaged in a $100 \times 100 \times 3$ pixel area forming a single bin. After that background and camera sensitivity corrections were applied. The resulting light distribution was checked for symmetry and fitted by the $\cos^n\theta$ function. In Fig. 2

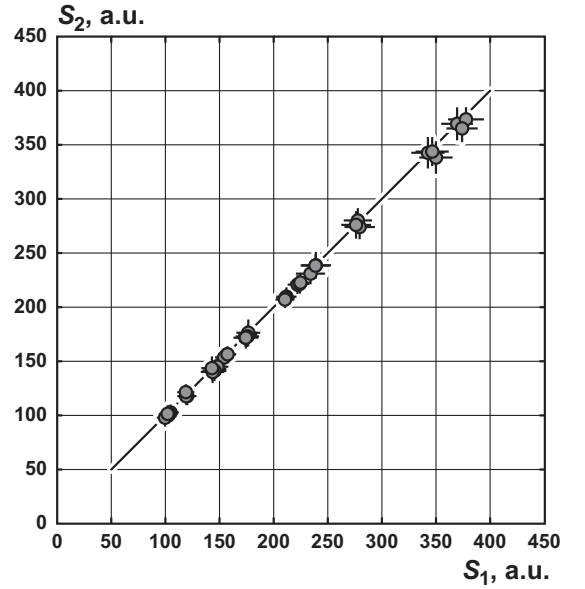


Fig. 3. The comparison of the two LED pulses amplitudes within the same 'calibration' frame. S_1 – amplitude of the first pulse and S_2 of the second pulse. Black line shows linear dependence $S_1 = S_2$.

the normalized intensity distribution is shown (black dots) along with the best fit with $n = 5.99 \pm 0.02$ (dashed line) for the optical fiber 1 (the values for other fibers are in a range from 5.5 to 6.7). The $\cos^2\theta$ comes from the geometry (since the screen is flat and camera sensitivity was already corrected), so our optical fibers on output have an angular distribution proportional to $\cos^\gamma\theta$, $\gamma=3.5$ – 4.7 . These values were then used to calculate the light distribution over the mosaic in the calibration pulses. The azimuth dependence of the light field was also checked and found to be less than 0.2% while the statistical uncertainty of signal measurement is about 1%.

3.2. LED pulse stability check

The overall calibration method is based on the assumption of LED flash stability, e.g. that a diode under fixed settings gives the same amount of photons in two consecutive flashes. To estimate the stability of the LED flash in laboratory conditions a series of 'calibration' frames was recorded. In this series all of the optical fibers were detached from the calibration board except one. This fiber was attached to the different LEDs one by one. Thus in this case in the 'calibration' frame only the pulses from a single LED were present, one pulse from time slots 1–7 and second one from time slots 9–15 (see Table 1). The pulses amplitudes were estimated. The signal amplitude estimation precision is about 0.3–0.7%. In Fig. 3 the results of comparison of two pulses amplitudes (S_1 and S_2) from the same frame are shown (dots). The black line represents the $S_1 = S_2$ case. In Fig. 4 the distribution of the pulse amplitude differences is shown. There is a systematic 1.1% difference between the first and the second light pulse intensity which is accounted for during the relative calibration. The LED pulse stability is about 1.2%.

Another estimation was done using data from experimental runs. From a series of 'calibration' frames that were recorded during a short time (relative to the average conditions change time) variation of individual pulse intensities was estimated. Comparison of all of the 'calibration' frames of one set of measurements during a single flight (flight No.1 in 2013) shows that the pulse intensity was stable even under varying conditions. Comparison of pulse intensity fluctuations in the Hamamatsu R3886 ($\sigma/S \sim 2\%$ in a single LED pulse and $\sim 1\%$ in the all-LED pulse, see Fig. 5) and FEU-84-

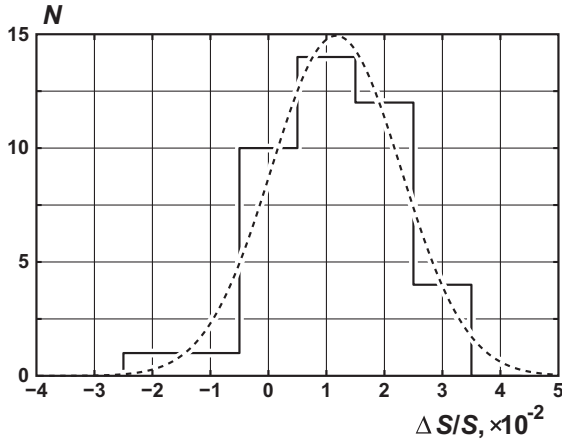


Fig. 4. Distribution of the relative difference between pulse amplitude from two consecutive individual LED flashes in the same 'calibration' frame in Hamamatsu R3886 PMT (histogram) with a Gaussian curve fit with a 1.1% width (dashed line).

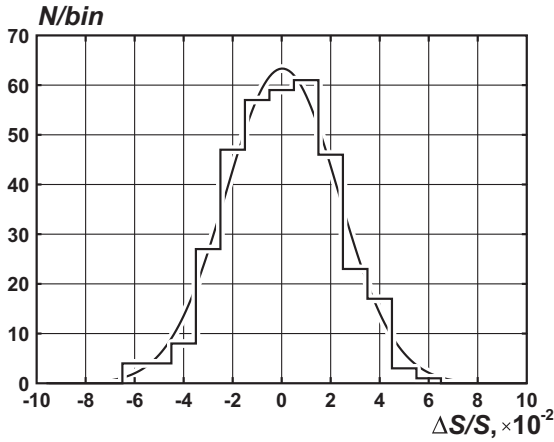


Fig. 5. Distribution of the relative difference between signals from LED flashes in two consecutive 'calibration' frames in Hamamatsu R3886 PMT (black histogram) with a Gaussian curve fit with a 2% width (curve).

3 (~3.5% and ~2% respectively) shows that the LED pulse intensity variation is comparable to the pulse intensity estimation error (0.3% for R3886 PMT and 0.5–1.1% for the FEU 84–3 PMT in the all-LED pulse). The long term stability of the LED may be checked comparing pulse amplitudes from random 'calibration' frame pairs, but this stability is not required for the relative calibration method used.

4. PMT mosaic calibration

4.1. PMT linearity check

The non-linearity of PMTs is a known problem. Data from the 'calibration' frame can also be used to check the PMTs linearity and subsequent correction. Since the frame consists of individual LED pulses and their combinations (see Table 1) one can check that a PMT's response is a linear combination of the responses to the individual pulses. So parallel to the relative calibration procedure (see below) the linearity check is done.

First, individual LED pulses are estimated (time slots 9–15). For this from the 30 bins of each pulse time slot only the 20 central bins are taken leaving out 5 at the very beginning and end of

the slot for any possible transition effects (the LED achieves its intended brightness not instantly but over about 30 ns what is equal to ~2 bins, and 1 bin for a possible timing uncertainty, plus 2 extra bins). For the measured value the average of these 20 measurements is taken. The individual LED flashes (slots 9–15) were taken as base or 'true' values S_i^j (j denotes slot number, i – PMT number). Then combinations for slots (1–7) were checked. e.g. if the PMT response is linear then the signal in the first two time slots will be equal to the sum of all signals from individual LED pulses, in the third time slot the signal should be equal to sum of signals from LEDs 1–6, and so on.

The result is shown in Fig. 6a. $S_{measured}$ stands for the signals from slots 1–7 (collective LED pulses), $S_{predicted}$ – for the corresponding sums of signals from slots 9–15 (individual LED pulses). Black dots represent the data for all FEU-84-3 PMTs, crosses for the Hamamatsu R3886. The dashed line shows the linear dependence. It can be seen that while FEU-84-3 shows little deviation from linearity (about 2–3%), the Hamamatsu R3886 shows significant non-linearity. This non-linearity comes from the PMT's power supply which is the same in design as the power supply sources of the FEU-84-3. But with the same voltage in the dynode system the Hamamatsu R3886 has a much higher amplification which with higher quantum efficiency can lead to FADC over saturation (all FADCs are equal). Thus in order to decrease its amplification the Hamamatsu R3886 was operated at a lower dynode voltage. Moreover to decrease the fluctuations and the FEU-84-3 PMTs' dark current the last three dynodes of each PMT in the mosaic were shunted together with the anode. This way of PMT powering is not standard and is described as unfavorable due to loss of linearity. For Hamamatsu R3886 when directly asked the manufacturer provided no guaranty of linearity. So the non-linearity was expected albeit not to this scale.

To solve this problem the signals in each PMT were corrected. The following correction was used:

$$S_{true} = S_{measured} (1 + \tau S_{measured}^{1/2} + \alpha S_{measured}),$$

where for FEU-84-3 $\tau \sim 4 \cdot 10^{-2}$, $\alpha \sim 3 \cdot 10^{-3}$. As the common high signal in the 'event' frames is about 100 a.u. the corrections are small.

The corrected linearity check results are shown in Fig. 6b. The deviation of each dot in the figure from the central line is less than the error of signal estimation. For further use all signals in the PMTs were corrected to ensure a linear response. It is worth noting that the linearity corrections of the signals in PMT 1 affect the overall results of the calibration procedure as the signals in other PMTs are normalized on the signal in PMT 1. However, the signals in the 'calibration' frame are high (higher than signals from EAS), thus the possible systematic uncertainty introduced by this procedure is less than the residual non-linearity (estimated to be about 0.2%), and thus is negligible.

4.2. Relative calibration

4.2.1. The method

Relative calibration of the PMT mosaic was done differently than the usual relative calibration in modern experiments [11–13]. This is due to the compact geometry of the detector, in which the incidence angles of rays falling from a certain optical fiber output on the farthest PMTs are high (see Fig. 1a) making reflectivity significant (along with small effective area of the PMT window). As a result, the uniform light source will still produce non-equal signals in the same PMT positioned in different places of the mosaic. So this part was replaced with signal normalization in which the signals were corrected to the expected ones based on the known uneven light distribution.

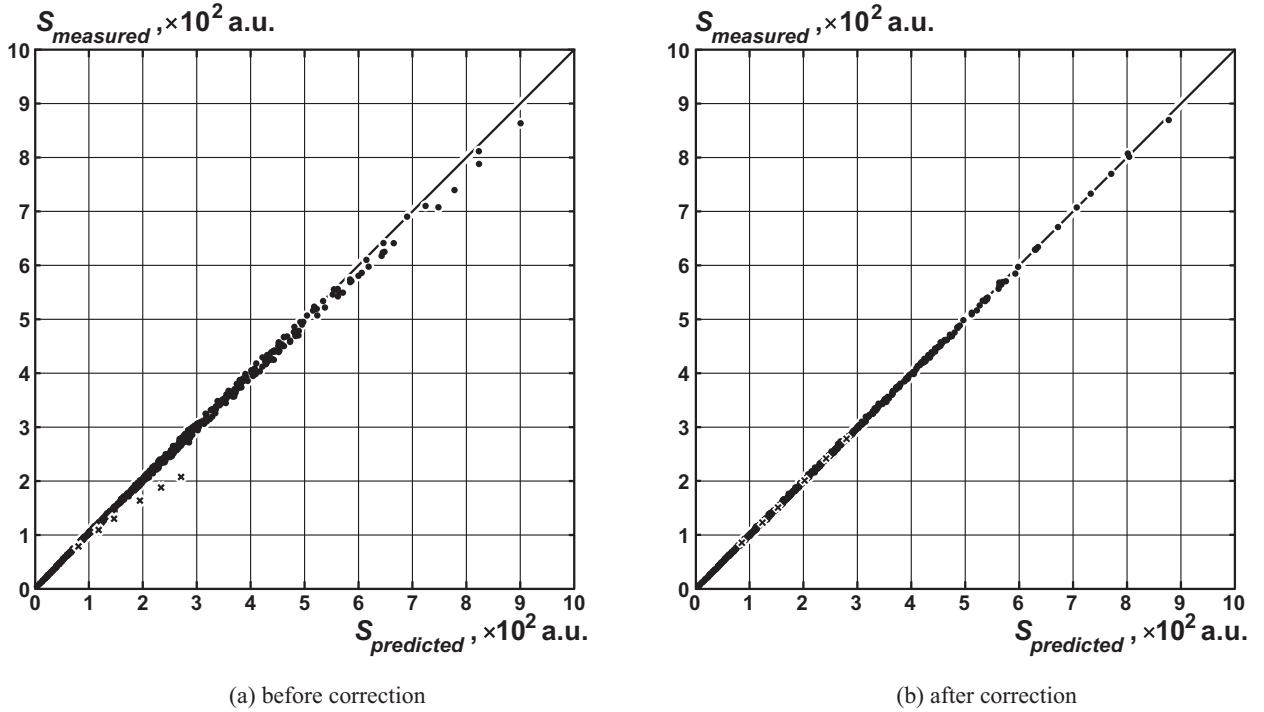


Fig. 6. Linearity check for all 109 PMTs used. Dots represent the data for FEU-84-3, crosses are for Hamamatsu R3886. The latter shows significant non-linearity and must be corrected. Linear dependence for reference is shown by the solid line.

Relative calibration was done for each ‘event’ frame using its paired ‘calibration’ frame. For each ‘calibration’ frame a set of calibration coefficients was estimated. The estimation was done based on three assumptions. First assumption, PMT 1 is stable and has the same sensitivity at any background lighting at a fixed voltage on the dynodes. This was checked under laboratory conditions, no variations exceeding signal estimation uncertainty were found. The only thing that remained uncertain was the possible sensitivity of the power source to the relative humidity, but this was estimated to have a very small effect. The temperatures of all power sources were monitored continuously and showed little variation (only a few degrees during flights). Second, it was assumed that in one frame two consecutive flashes of the same LED are of the same intensity (this was checked as described above). Third assumption was that the PMTs’ sensitivities vary much slower than the 18 μ s delay between the event and calibration sequence.

4.2.2. Relative calibration procedure

Since the geometry was fixed and known for each LED (see Fig. 1 for LED positioning), the distribution of light from that LED across the mosaic can be calculated taking into account the reflection from the PMT’s glass surface. Using this distribution the signal D_i^j from a certain LED j in each PMT i was calculated. After that, the signals D_i^j were normalized to the signals in PMT 1 D_1^j , giving the relative signals $A_i^j = D_i^j/D_1^j$ ($A_1^j = 1$). It is worth noting that the only difference at this step from the commonly used relative calibration procedure is that A_i^j cannot by all means be made equal to 1 in our geometry. In most of the recent fluorescent or imaging atmospheric Cherenkov telescopes a considerable effort is made to ensure that the relative calibration light field distribution is uniform or close to uniform.

Next, the brightness of each LED was assumed equal to the signal, which was generated by its individual flash in PMT 1 (S_1^j – the measured signal in PMT 1) during time slots 9–15 of the ‘calibration’ frame with the 1.1% correction (see Section 3.2). Then the theoretical signal in each PMT was estimated using these rela-

tive signals A_i^j as $T_i^j = A_i^j \times S_1^j$. For time slots 1–7, where the LEDs were fired in combination, the signals were estimated as a sum of individual light pulses, e.g. for time slot 7 the signals will be $T_i^7 = A_i^1 \times S_1^1 + A_i^2 \times S_1^2$ and so on.

Finally, the calibration coefficient for each PMT C_i was estimated as the ratio between the predicted integral signal over the full calibration frame, using all of the theoretical signals T_i^j summed together over all pulses, and the measured one.

4.2.3. Relative calibration verification

The next step was to check the validity of this calibration since the relative calibration was done in automatic mode and was not checked manually later. For this the calibration coefficients were applied to a ‘calibration’ frame. Then, since the light distribution over the PMT mosaic was smooth and transition areas between pulses were about 2–3 bins wide, the ‘time-space’ smoothing filter was applied. In each PMT for each time bin the signal was averaged with different weights with the signals in this and the neighboring PMTs in this time bin and the signals in this PMT in two previous and two following time bins. This procedure reduces the possible noise and strongly affects incorrect values (if there were any). After this new calibration coefficients were estimated by the same way as the first set. The new coefficients were expected to be very close to 1, if the initial calibration was accurate. Or differ by more than 0.05 from 1, if something went wrong (a clipped calibration frame due to delay line malfunction, or the PMT was highly unstable due to power supply source failure and etc.).

4.2.4. Relative calibration uncertainties

The uncertainty of the relative calibration comes from several sources.

First, the LEDs pulse stability was found to be 1.2%. So for the full ‘calibration’ frame the uncertainty from the LEDs instability is about 0.44%.

Second, uncertainties in the parameters of the angular distribution of the optical fibers. It should be noted that the uncertainty

in the power index γ of the fit presented in Fig. 2 represents the fitting procedure uncertainty only. Additional uncertainties of the image processing (including the background and camera sensitivity corrections and the geometrical uncertainties) introduce much higher uncertainties. However, the models show that the reconstructed relative calibration coefficients for a given event (from experimental runs) using light fields calculated with an angular distribution $\cos^\gamma\theta$ where $0 \leq \gamma \leq 8$ (at $\gamma = 0$ the fiber angular distribution is uniform and at $\gamma = 8$ the fiber produces a narrow beam, two extreme cases) show variation only about 25% between the extremes (the effects of the detector geometry). The change of γ from 4.0 to 5.7 changes the resulting calibration coefficients by 2% on average and 7% maximum. In our case the fibers' angular distribution was measured with relatively good precision, the uncertainty in the power index of the angular distribution is about 0.5–0.7. For this level of uncertainty in the angular measurement the resulting uncertainty of the relative calibration coefficients is below 2%.

Third, uncertainties in the optical fiber positioning. The actual positions of the fibers on the mirror were well measured, but their directions were less well known (no better than 1.5°). The models show that this uncertainty may add up to 3–10% difference in the reconstructed relative calibration coefficients. But these uncertainties tend to produce a higher systematic shift in the lateral PMTs rather than in the central ones or produce local shifts in a few PMTs. The local systematic shifts will result in groups of points to be constantly shifted on the reconstructed LDFs. We observe no groups or isolated points with constant shifts higher than 5% on our LDFs, but a careful analysis may provide a better estimation. The radial dependent systematics are harder to identify. This kind of systematic uncertainty produces leads to the spreading of the LDF points for the on-edge events. Such systematic shifts are detected and corrected at the LDF reconstruction and analysis.

Next, the signal measurement accuracy affects two things: first, the precision of signal reconstruction in each channel and second, and more vital, the precision of LED pulse intensity reconstruction using data from PMT 1. Signal measurement error in PMT 1 in each pulse in our case is from 0.8% to 2% depending on pulse number. Overall precision of signal reconstruction in other PMTs is from 1.2% to 4%. The LED stability is higher than this (see Section 3.2). So the estimated precision of the 7 LEDs' combined flash is 2.6%. This results in a 3% overall statistical accuracy of the relative calibration plus 5% of the systematical uncertainty.

This agrees with the precision estimation results obtained from comparing of pairs of 'calibration' frames registered one right after the other. The average difference between the relative calibration coefficients in each PMT (except for a malfunctioning one) is less than 3%. So we consider the accuracy of the relative calibration to be 3%.

4.3. Absolute calibration

The DAQ system measures the voltage on the load resistor in the PMT chain in arbitrary units ('code' units). So it is necessary to determine the amount of photons on the photocathode that corresponds to one 'code' unit in the output. One 'code' unit is equal to a 2 mV step on the FADC input. Taking into account the amplifier coefficient of 30 and the fact that only half of the anode current flows through the load resistor [7], one 'code' unit is approximately equal to a $2.67 \mu\text{A}$ current through the PMT's anode. Thus for a 12.5 ns integration this gives 33 fC of charge. So the task is to measure the number of photons that generate a given charge on the anode output.

For this a Hamamatsu L11494-430 stabilized light source [15] with emission intensity of 1.002 pW ($\sim 2.12 \cdot 10^6$ photons per sec-

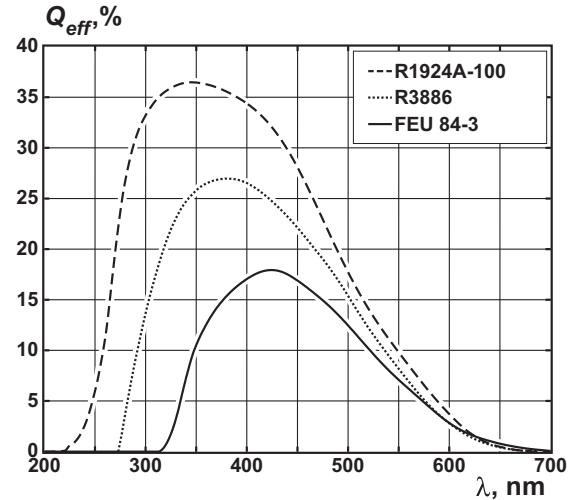


Fig. 7. Typical quantum efficiency spectral profile of Hamamatsu R1924A-100 (dashed line) [6], Hamamatsu R3886 (dotted line) [6], typical FEU 84-3 (solid line) [5].

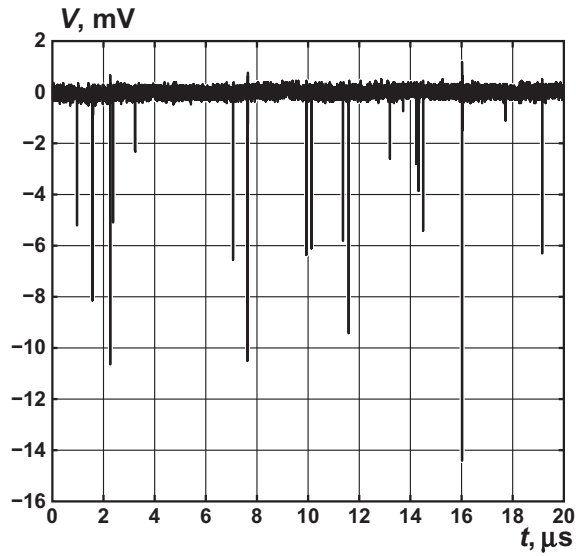
ond) in the HI mode was used. The diameter of the emission area of the light source was 7 mm, the emission peak maximum was at 430 nm, spectral line FWHM was 65 nm and the stability was $\pm 2\%$ (manufacturer provided data).

4.3.1. Intermediate PMT calibration

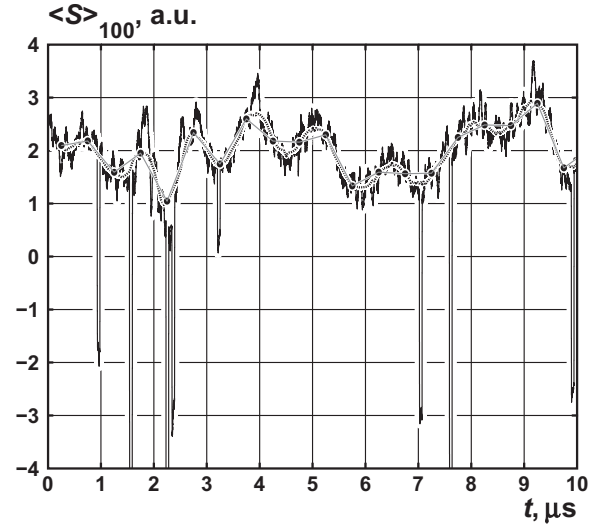
Unfortunately the design of the PMTs' power sources used in the SPHERE-2 apparatus does not allow to achieve the maximal amplification with the Hamamatsu R3886 PMT and to set it into photon counting mode, thus making it impossible to calibrate it with the L11494-430 light source. So the absolute calibration of the Hamamatsu R3886 PMT was done using another highly sensitive PMT – Hamamatsu R1924A-100 powered via the manufacturer recommended scheme. Though the actual values of the quantum efficiency of this PMT (35%) are higher than those of Hamamatsu R3886 (24%) and FEU-84-3 (18%), the maximums of R1924A-100 and R3886 quantum efficiency curves are near 400 nm (see Fig. 7), e.g. are in the same wavelength region. So the idea was to measure the quantum efficiency and amplification coefficient of the R1924A-100 PMT and use it in turn to calibrate a brighter blue light source, which was then used to calibrate the Hamamatsu R3886 PMT.

In order to measure the quantum efficiency of the Hamamatsu R1924A-100 PMT, it was set into the maximum amplification mode and brought into contact with the light source working in the continuous emission mode. Then 20 oscillograms of the voltage on the load resistor in the PMT chain were registered with an external LeCroy WaveJet oscilloscope. Each oscillogram was 200 μs long at a 2 Gs/s rate (e.g. 0.5 ns discretization). In Fig. 8a part of such oscillogram is presented. Single photoelectron peaks can be clearly seen, the minimal distance between two peaks was about 100 ns, e.g. no overlapping was observed.

In Fig. 8b the same oscillogram averaged over 50 ns is shown. The baseline voltage variations can be clearly seen. These variations come from numerous sources (the variations of the power supply grid, radio emission of numerous phones and wireless devices nearby etc.). The baseline variations were estimated to have a very low impact on the photoelectron effective charge estimations (the photoelectrons, as follows from the averaged signals, produce 200–800 times higher voltage pulses), but they strongly widen the noise peak around the true zero and thus may affect the estimation of the number of photoelectrons. The baseline was corrected using two different approaches: using local data and using contin-



(a) unaltered voltage profile



(b) averaged over 50 ns

Fig. 8. The oscillogram of the voltage impulses on the Hamamatsu R1924A-100 anode collected when lighted by the Hamamatsu L11494-430 light source. The right figure shows baseline fluctuations of the same oscillogram on the left. Black line shows the averaged over 100 time bins (50 ns) voltage oscillogram, gray line with dots show linear baseline approximation, while dotted line presents continuous baseline approximation (see text). 1 a.u. is the ADC step and is equal to 62.50 μV . (For interpretation of the references to color in this figure legend, the reader is referred to the web version of this article).

uous smoothing. For the local data approach (gray line with dots in Fig. 8b) the oscillogram was divided into 500 ns long parts. For each part the distribution of the voltage values was fitted with a Gaussian distribution. The mean values were assigned to the center points of the respected oscillogram parts (shown in the figure as dots). The baseline value for other points was linearly interpolated. This approach allowed to better estimate of the charge under the single photoelectron peaks. But even better results were achieved using continuous baseline approximation. This approximation was built for each point of the oscillogram (except the edges) as the mean value of the recorded voltage within the 500 ns part excluding values laying more than 10 a.u. from the average (approximately 3σ of the noise). This approximation is shown as the dotted line in Fig. 8b). For further analysis the baseline was subtracted from all recorded oscillograms. The average residual baseline uncertainty is estimated to be less than 0.1 a.u., e.g. 6.25 μV . But it adds as a random error and does not add to the systematical error.

These voltage oscillograms then were converted to anode current oscillograms. Then, for any current value everything around with the same sign (e.g. in between the two changes of the current sign) was assumed to be a single peak. By integrating the area under these peaks the charges were obtained and their distribution was built. In that distribution the main peak around zero presented the noise. The positive collected charges were produced by random noise, the negative charges were produced by random noise and photoelectrons. The noise peak was assumed to be symmetrical and the positive part of the charges distribution was subtracted from the negative. The resulting distribution is shown in Fig. 9. In the left part of the figure are the omitted residual noise peak values (crosses), in the center is the single photoelectron maximum (black dots) and on the right is the omitted part from particles (crosses), that were observed even when the light source was turned off. The dashed line in the figure represents the Gaussian fit of the photoelectron peak.

From this fit the number of photoelectrons (3176 ± 78) and the average charge on the anode from a single photoelectron (0.499 ± 0.003 pC) were obtained. This number of photoelectrons was ob-

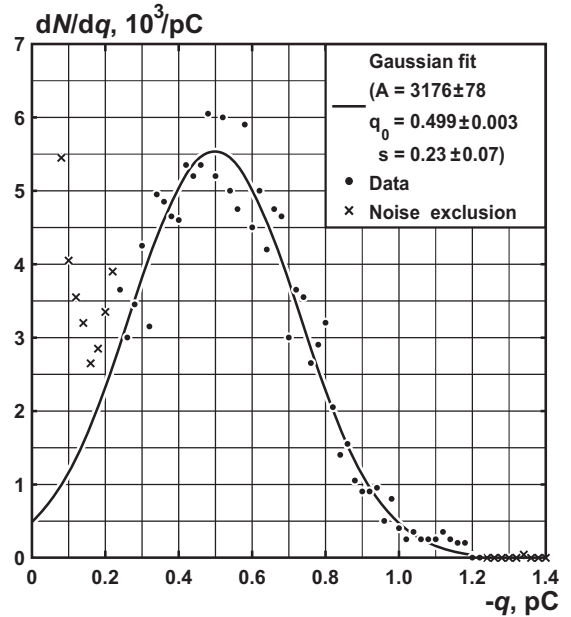


Fig. 9. Distribution of the charges produced by a single photoelectron. Dots present data, crosses present omitted noise peak, the black line presents the Gaussian distribution approximation (the parameters are given in the top-right corner).

tained from 20 oscillograms over a total time of 4 ms. During this time the light source should have emitted 8480 ± 150 photons. The PMT's photocathode dark current according to manufacturer-provided test sheet is 1.30 nA. For 4 ms this gives accumulated 5.2 pC charge of 10 photoelectrons due to thermoemission. Thus the quantum efficiency of the PMT in question was $37.3 \pm 1.1\%$ (relative uncertainty 3%) for the emission line 430 ± 33 nm. The absolute sensitivity of the PMT was calculated as the number of photons in one arbitrary unit, e.g. as the product of the quantum efficiency and the amplification coefficient of the dynode system. The amplification of the dynode system can be derived from the

manufacturer provided PMT test sheet as the ratio of the anode luminous sensitivity (316 A/lm) to the cathode luminous sensitivity (102 μ A/lm) or as the ratio of the mean charge of a single photoelectron peak to the electron charge. From the manufacturers data the PMT dynode system amplification is $(3.10 \pm 0.03) \cdot 10^6$. From our measurements the PMTs amplification was $(3.115 \pm 0.003) \cdot 10^6$. The two values are in a very good agreement. For the Hamamatsu R1924A-100 PMT in maximum amplification mode it was found to be 5.37 ± 0.16 photon/pC for the 430 ± 33 nm emission line.

4.3.2. R3886 PMT calibration

To estimate the sensitivity of the Hamamatsu R3886 PMT (the one, used as stable in the experimental run) both PMTs were positioned close to each other at about 40 cm from a LED light source. This LED was similar to those used in the experiment with emission maximum at wavelength of 405 nm and a 15 nm line half width [8]. The LED was covered by a spherical Lambertian diffuser and each PMT was covered with a diaphragm with a 6 mm hole to ensure that, first, both PMTs will receive the same amount of light since R3886 and R1924A-100 have different photocathodes diameters (34 mm and 22 mm respectively) and, second, that R1924A-100 photocathode will be illuminated on the same area, that was used during its absolute calibration. The Hamamatsu R1924A-100 PMT was set under the same conditions as in the calibration measurements above and the Hamamatsu R3886 PMT was set to maximal amplification allowed by its normal power source. A series of 30 μ s LED flashes was fired and the PMTs' outputs were recorded by the same external LeCroy WaveJet oscilloscope.

The quantum efficiency of the Hamamatsu R1924A-100 PMT at 430 ± 33 nm is lower than at around 405 nm (see Fig. 7). The effective quantum efficiency for 405 ± 15 nm LED is by 15% higher (typical 34.3% against typical 29.0% and we have a sensitive in blue area PMT according to its manufacturer-provided testing sheet). The uncertainty of this estimation is discussed below. This correction was applied in further calculations (e.g. 4.54 ± 0.14 photon/pC at 405 ± 15 nm for R1924A-100). Since the PMTs are connected to DAQ via relatively long well measured cables (2 m), the cables have a different resistance for short and long pulses (see [7]), what results in a 7% less measured current for long pulses (single photoelectron) meaning 4.84 ± 0.15 photon/pC for long pulses (relatively long LED pulse). From the total amount of charge (243.23 ± 0.33 nC including baseline estimation uncertainty) collected from the Hamamatsu R1924A-100 PMT during 30 μ s pulses the number of photons that fell on its photocathode was estimated to be $(1.178 \pm 0.036) \cdot 10^6$. Assuming that the same number of photons fell on the Hamamatsu R3886 photocathode, for the total collected 17.40 ± 0.04 nC charge its sensitivity was estimated to be 67.7 ± 2.1 photon/pC for a 405 ± 15 nm LED emission line.

To ensure the correct results of the R3886 PMT calibration its photocathode was checked for zone sensitivity variations as the measurements above were taken for a 6 mm diameter center area only. For this test the PMT was illuminated by a copy of the calibration board equipped by the 7 LEDs with different emission line mean wavelengths (from 405 up to 660 nm) and widths (from 15 up to 65 nm). For the light source stability control the second PMT was installed near the first one. The light source was installed behind two Lambertian diffusers set 2 cm apart of each other. A 6 mm diaphragm was positioned in the center and at 4 points near the edge of the photocathode. For each diaphragm position 3 series of light pulses were recorded (see Table 1 for pulse pattern) using a LeCroy WaveJet oscilloscope. The amplitudes of the reconstructed light pulses S_i show small variations for different diaphragm positions. No systematic change in reconstructed signals was observed. In Fig. 10 the distribution of signals deviation from mean is shown along with its Gaussian fit. The average deviation is

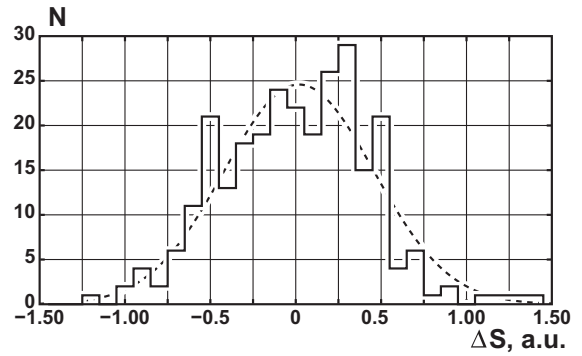


Fig. 10. The histogram of deviations from mean of signals measured during Hamamatsu R3886 zone sensitivity check (black line) along with its Gaussian fit (dashed line). Fit with is about 0.5 a.u., signal estimation uncertainty about 1 a.u.

Table 2

Hamamatsu R3886 sensitivity at different voltages. Third column lists photons from calibration LEDs, fourth column lists 'ideal' (see text) Vavilov–Cherenkov photons in the 200–700 nm wavelength range.

Voltage code	Collected charge, nC	Sensitivity photon/pC	Photons in 'code' unit
255	30.28	67.7	5.33 ± 0.16
150	11.01	189	14.32 ± 0.44
106	7.61	269	20.7 ± 0.6
69	5.65	362	27.9 ± 0.9
63	5.44	377	29.0 ± 0.9
50	4.98	412	31.7 ± 1.0
0	3.81	538	41.4 ± 1.3

about 0.5 a.u. while the estimated uncertainty in the signal reconstruction is about 1 a.u. (0.8–1.1 a.u.). So the we assumed Hamamatsu R3886 photocathode to have equal sensitivity in each point in the 400–670 nm wavelength range.

In experimental runs the voltage on the Hamamatsu R3886 dynode system was set automatically to suit the flight conditions and the voltage was always much lower than the maximum possible. In order to measure the sensitivity at lower voltages another series of LED flashes was made. The flash intensity was controlled with the Hamamatsu R1924A-100 PMT via the same oscilloscope. But the signal from the Hamamatsu R3886 PMT was recorded by the detectors of the DAQ system and with the LeCroy WaveJet oscilloscope in parallel. With fixed LED flash brightness (the total number of emitted photons estimated as $(2.08 \pm 0.06) \cdot 10^6$) the dependence of the charge collected from Hamamatsu R3886 from the voltage on its dynode system was measured. The calibration results are given in Table 2. In the third column the sensitivity to the 405 nm LED photons are given as obtained from the calibration procedure.

To estimate the number of Vavilov–Cherenkov photons in the 200–700 nm wavelength range in a unit of charge, the response ratio to an average LED photon and an average Vavilov–Cherenkov photon was calculated using the PMTs' photocathode quantum efficiency wavelength dependence profiles. This ratio was about 2.33 for Hamamatsu R3886 and 2.18 for FEU-84-3 and thus the actual numbers of photons in the real observations were respectively higher (for the Hamamatsu R3886 PMT see fourth column in Table 2). However, the presented values were calculated for an 'ideal' Vavilov–Cherenkov spectrum (that is $J \sim 1/\lambda^2$). The real spectrum of Vavilov–Cherenkov photons from EAS depends on the shower primary energy, type and zenith angle and can be obtained from the simulations, thus the number of Vavilov–Cherenkov photons depends on the shower parameters.

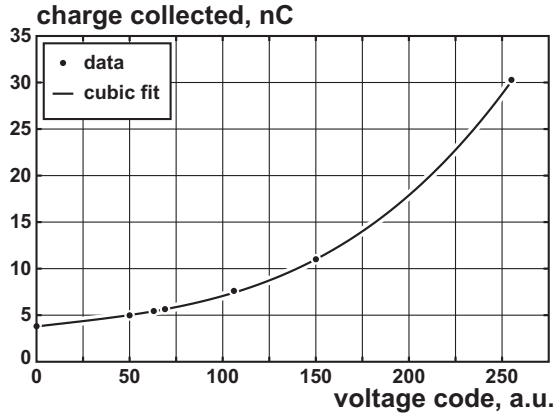


Fig. 11. The Hamamatsu R3886 PMT sensitivity curve: dots represent measurements, solid line represents cubic fit.

The real voltages in the 2013 experimental run were between code 59 and code 89 thus giving us an average of 24 photons per 'code' unit (see Fig. 11).

4.3.3. Absolute calibration uncertainties

The Hamamatsu R3886 absolute calibration procedure uncertainties come from several sources.

First, the Hamamatsu L11494-430 light source has stability of 2%. Any uncertainty in the number of photons this light source produce affects the results of the absolute calibration giving systematic shift, thus adding 2% systematic uncertainty.

Second, the uncertainty in the number of photons that fell on the R1924A-100 and R3886 PMTs photocathodes during the calibration. The main source of this uncertainty is the misalignment of the LED. The shift of the PMTs by 10 mm (and this is twice higher than the PMT positioning precision) orthogonally to the light source direction results in 0.13% difference in the number of collected photons. This is a small uncertainty compared to other sources. The diaphragm diameter uncertainty was about 0.02 mm and the resulting uncertainty of diaphragm area was 0.7%.

Third, the spectral dependence of the Hamamatsu R1924A-100 quantum efficiency is taken from the manufacturer provided datasheet. The manufacturer's test results state that the PMT has a cathode blue sensitivity index of 14.60, while a typical PMT of this model has blue sensitivity index of 13.50. The blue sensitivity index is a cathode current produced by a normally powered PMT illuminated with tungsten lamp at 2856 K through a Corning CS 5-58 optical filter polished to the half-stock thickness. This filter has a transparency window at 405 nm with a 42 nm half width (plus some transparency in the near infrared region) with peak transparency of 60%. This effectively produces the light source with a 430 nm mean wavelength and a 35 nm half width peak. This means that our Hamamatsu R1924A-100 PMT is more sensitive in the blue area than a typical one. The PMTs datasheet also states that the PMTs cathode is 8% less sensitive to the broad spectrum of the above mentioned tungsten lamp (which has a maximum in infrared region). With high measured quantum efficiency to the 430 nm light source, this means that our PMT has a quantum efficiency curve significantly different in shape, than the typical one, with higher sensitivity in the blue and violet region and lower in the red spectrum region. This may lead to incorrect estimation of the PMT sensitivity to the 405 nm LED photons using the sensitivity to the 430 nm photons (with account for their line width).

However, we performed a test of the PMT response dependence on the wavelength using the same setup which was used to check the Hamamatsu R3886 PMT zone sensitivity. In the first series of

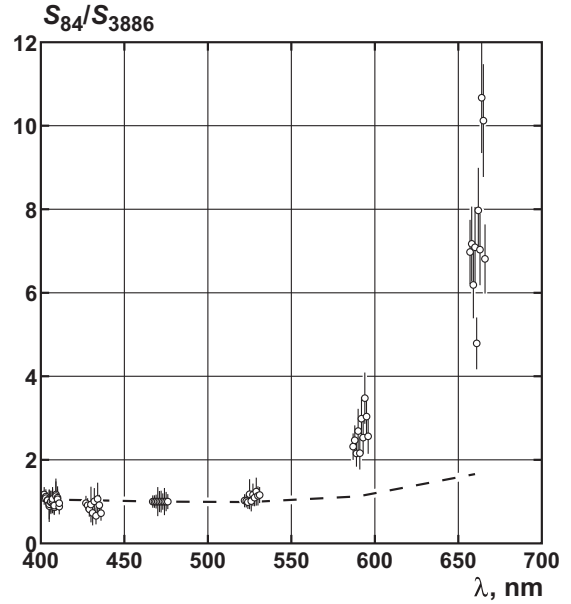


Fig. 12. The comparison of the FEU 84-3 and Hamamatsu R3886 PMTs sensitivity to different wavelength LED pulses. The signal ratios are normalized to the signal ratio at 475 nm, as the PMTs have different amplification. The dashed line represents power estimated signals ratio from quantum efficiency curves (see Fig. 7).

measurements the Hamamatsu R3886 and a number FEU 84-3 PMTs were illuminated by the different LED pulses. The LEDs used had the following emission lines (the mean wavelength and line half width are listed): 405 ± 15 nm, 405 ± 33 nm, 430 ± 39 nm, 470 ± 27 nm, 455 ± 26 nm, 590 ± 17 nm, 660 ± 14 nm. The LED properties were taken from manufacturers data sheet [16]. The signals from the PMTs were registered using both channels of the oscilloscope. Thus each LED pulse was registered by both PMTs simultaneously allowing direct comparison of the registered signal amplitude. The results of this comparison are presented in Fig. 12. The plot shows measured signal pulse amplitudes in FEU 84-3 and R3886 PMTs. The ratios are normalized to the ratio for a 475 nm LED. The line on the plot presents expected ratio calculated using quantum efficiency spectral dependencies (see Fig. 7). In the 400–500 nm region the expected and measured ratios are in a relatively good agreement. In the long wavelength region the agreement is very poor, meaning high FEU 84-3 PMT sensitivity to the red photons.

The same test was done for the Hamamatsu R1924A-100 and Hamamatsu R3886 PMTs pair. The results are presented in Fig. 13. The measured ratios are in a good agreement with the expected ones except for the long wavelength area where both PMTs have a low quantum efficiency. Also Hamamatsu R1924A-100 PMT from the manufacturer's test is expected to have a lower quantum efficiency than the typical PMT of that type. The measured signal ratio for the 430 nm LED is 1.025 ± 0.06 and the expected ratio is 1.077. For the 405 nm LED (the same to ones used in calibration board) the measured signals ratio is 1.024 ± 0.08 and the expected one is 1.107. Thus, we assume that the manufacturer provided quantum efficiency spectral curves are correct (except of the FEU 84-3 PMTs in the red area). Then the 15% correction applied to the Hamamatsu R1924A-100 PMT sensitivity between Hamamatsu L11494-430 light source and calibration LED is estimated correctly and adds a 6% systematic uncertainty.

The uncertainties in the LEDs properties do not affect the absolute calibration results directly, but introduce uncertainties in the quantum efficiency spectral curve check. However, the variation of the mean wavelength by about 15 nm results only in a 3% change

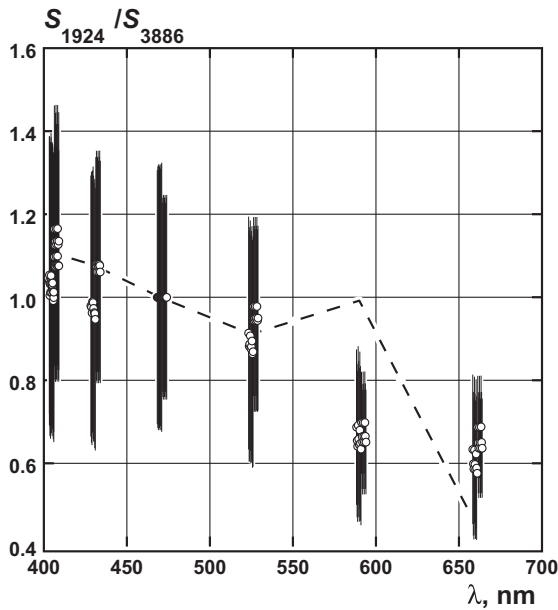


Fig. 13. The comparison of the Hamamatsu R1924A-100 and Hamamatsu R3886 PMTs sensitivity to different wavelength LED pulses. The signal ratios are normalized to the signal ratio at 475 nm, as the PMTs have different amplification. The dashed line represents power estimated signals ratio from quantum efficiency curves (see Fig. 7). (For interpretation of the references to color in this figure legend, the reader is referred to the web version of this article).

in the expected signal. The same is true for the LED emission line half width, the widening of the line by 10–15 nm result only in a 2–3% change in the expected signal. The uncertainties of the signal estimation were about 10%–20% and thus the LED's parameters uncertainties have small impact.

Another source of uncertainties is the state of the PMT power supplies and their temperature. During all tests in the laboratory the Hamamatsu R1924A-100 PMT was powered by a manufacturer recommended scheme. The voltage on the dynode system was controlled with 0.5 V precision at 1250 V, thus the variations in PMT gain were less than 0.1% according to the manufacturer provided data. The Hamamatsu R3886 PMT was powered using the detectors default power supply. The voltage on the PMT was monitored and showed variations ~ 1.2 V at 950 V, the gain variations were less than 0.2%. All measurements were performed after the PMTs were kept in a dark environment overnight and powered for more than 30 min. The temperature of the PMTs was not monitored, but there were no large variations in the room temperature during and between measurements. So we assume the uncertainties coming from PMT state to be negligible.

However, the temperature and voltage on the Hamamatsu R3886 dynodes fluctuated during the flights. The average voltage fluctuations from the mean value were about 6–7 V and temperature variations of the PMT were 5–10 °C. The variation in the R3886 PMT gain caused by these voltage fluctuations were about 4.3% according to the manufacturer provided data. The variation of the PMT gain caused by the temperature variations are a more complex subject as the sensitivity temperature coefficient is wavelength dependent above 550 nm (-0.4 %/°C below 550 nm). Most of the Vavilov–Cherenkov photons have short wavelengths so we estimate the uncertainty from the temperature variations to be about 3%. The SPHERE-2 detector telemetry contains all of the necessary data for an event-by-event correction of these fluctuations, but a careful analysis is yet to be done.

Next, the uncertainty in the estimated number of Vavilov–Cherenkov photons in 1 'code' unit for FEU 84–3 PMT caused

Table 3
The calibration procedure uncertainties breakdown.

Source	statistic, %	systematic, %
Relative calibration		
PMTs residual	0.3	0.1
non-linearity		
LED pulse stability	0.5	–
Calibration pulse	2.8	–
intensity estimation		
Light distribution over mosaic uncertainty	–	5.1
Absolute calibration		
L11434-940 output	–	2.0
stability		
R1924A-100 quantum efficiency estimation	–	3.0
R1924A-100 gain stability	–	0.1
R3886 calibration		
Calibration pulse estimation precision	–	0.3
Calibration LED misalignment	–	0.1
Diaphragm size	–	0.7
In-lab PMT gain stability	–	0.2
Correction on quantum efficiency spectral dependencies	–	6.3
FEU 84–3 red sensitivity correction	–	3.0
R3886 in flight		
Temperature instability	3.0	–
Dynodes voltage instability	4.3	–
Total	6.0	9.4

by the higher than expected PMT quantum efficiency in the long wavelength area results in a 5–10% uncertainty (individual for each PMT). This uncertainty can be corrected using the same method of signal ratios comparison adding a 3% systematic uncertainty to the PMT absolute sensitivity.

The overall precision of the absolute calibration of Hamamatsu R3886 is about 3% what gives a 6% precision of the absolute calibration of every other PMT in the mosaic with a 10% systematical uncertainty (see Table 3).

5. Discussion

The presented LED calibration method is suitable for any other experiment which utilizes tight PMT arrays. This particular method features a few advantages and a few drawbacks comparing to the ones used at Auger [9] or MAGIC [13].

The main difference of this implementation of calibration method is that the relative calibration is done differently. Instead of illuminating the PMT mosaic with a uniform light field and expecting the collected number of photons to be equal, this method relies on a modeled light distribution with account of reflections from PMTs surfaces. In our detector the mirror (and optical fiber outputs) are positioned close to the PMTs (see Fig. 1b) and hence the incident angles are high enough for reflectivity from the PMT glass to become significant and the effective PMT window surface to become much smaller. In this case the fiber output angular uniformity will not mean equal signals in PMTs. So the relative calibration becomes more complex.

The main drawback of the current realization of this method is that all of the calibration measurements were made with light sources (specific or just LEDs) in a relatively narrow wavelength region (400–430 nm). The Vavilov–Cherenkov radiation has a continuous spectrum, which in the air spans approximately from 250 nm up to 900 nm (and further, but that region is rarely used for EAS

registration). So if all of the calibration procedures are done at the same wavelength, but the PMTs have different quantum efficiency wavelength dependencies, then the calibration will be wrong in terms of the reconstructed number of Vavilov–Cherenkov photons. This possible error however did not appear in our data since the reconstructed Vavilov–Cherenkov radiation photons lateral distribution functions (LDFs) did not show any systematically misplaced points (which would have indicated such a problem).

In any case this drawback can be corrected by introducing several LEDs with different wavelengths into the calibration system. Mainly they should flash from the same optical fiber to have an exactly the same light distribution over the mosaic and hence give a relative spectral calibration with respect to the same central stable PMT, that can be calibrated later under laboratory conditions. These LEDs should add only a single line each without the need to reproduce the whole calibration pattern. And this improvement will be made in the next version of the SPHERE detector.

The main advantage of this method comparing to the one from the Auger experiment is that the relative calibration is made in each event rather than at the beginning and end of the night or at some fixed large intervals. During the night we observed changes in the dark current of our PMTs (about 20% variation) caused by changes in background lighting. Also some variation was observed due to temperature variations, but they were small. There is a strong (though not linear) correlation between the dark current and our PMTs' sensitivities. This is true for most of the old multi-alkali photocathodes, which is a result of photocathode aging [17]. So control of the PMTs' relative calibration in each event not only gives high calibration precision, but also allows to use cheaper and older PMTs in the mosaic.

6. Conclusion

The method of calibration used in the SHPERE-2 detector was based on an on-line relative calibration and subsequent absolute calibration. The presented method allowed to check for PMTs non-linearity and its subsequent correction. Relative calibration of the PMT mosaic allowed to achieve a 3% accuracy. Absolute calibration had a 3% statistical and a 6% systematic error. So the overall accuracy of the calibration procedure is 6% statistical plus 10% systematic error. Additional analysis of the reconstructed LDFs and direct measurement of the Hamamatsu R3886 and FEU 84–3 PMTs quantum efficiency spectral profiles can significantly enhance the precision of the calibration procedure.

Acknowledgments

The reported study was funded by the RFBR according to research projects no. 11-02-01475a, 13-02-00470a.

References

- [1] R. Antonov, S. Beschapov, E. Bonvech, D. Chernov, T. Dzhatdov, M. Finger, M. Finger, V. Galkin, N. Kabanova, A. Petkun, D. Podgrudkov, T. Roganova, S. Shaulov, T. Sysoeva, Results on the primary CR spectrum and composition reconstructed with the SPHERE-2 detector, *J. Phys.: Conf. Ser.* 409 (2013) 012088. IOP Publishing.
- [2] R. Antonov, T. Aulova, E. Bonvech, D. Chernov, T. Dzhatdov, M. Finger, M. Finger, V. Galkin, D. Podgrudkov, T. Roganova, Event-by-event study of cr composition with the sphere experiment using the 2013 data, *J. Phys.: Conf. Ser.* 632 (1) (2015) 012090.
- [3] A. Chudakov, The possible method of EAS registration based on Cherenkov light reflected from snow surface, in: Proceedings of All-Union symposium on cosmic rays 1972 (in Russian), Yakutsk office of Siberian Branch of Academy of Science USSR, 1974.(in Russian)
- [4] A. Anohina, R. Antonov, E. Bonvech, D. Chernov, V. Galkin, M. Panasyuk, V. Prosin, D. Pushkarev, S. Shaulov, F. Shihaliev, T. Sysoeva, B. Sabirov, L. Tkachev, F. Mir, F. Mik, M. Sonsky, Experiment SPHERE-2 status 2007, in: Proceedings of the 30th ICRC, Mexico City, Mexico, vol. 5, 2008, pp. 945–948.
- [5] M. Dunaevskaya P.V. Podoksina, J. Ronkin, Photoelectron multiplier FEU-84, *Prib. Teh. Exp. (in Russian)*. 5 (1970) 252–255.
- [6] K.K. Hamamatsu Photonics, Product specification., 2010. <http://www.hamamatsu.com/resources/pdf/etd/R3886AT9P8M0H1076E02.pdf>.
- [7] D.V. Chernov, R.A. Antonov, E.A. Bonvech, A.V. Shirokov, Optical and data acquisition system for the SPHERE-2 detector, in: C. Rogelio, J.C. Dolivo, G. Medina-Tanco, L. Nellen, F.A. Sanchez, J.F. Vald-Galicia (Eds.), Proceedings of the 30th International Cosmic Ray Conference, Mexico City, Mexico, vol. 5 (HE part 2), 2008, pp. 941–944.
- [8] Ningbo Foryard Optoelectronics., Product specification, 2013. foryard.com/x-en/p-download/d-Part/u-f/m-1/n-FFYL-5013VC1C/y-196f9.
- [9] A. Rovero, P. Bauleo, J. Brack, J. Harton, R. Knapik, Multi-wavelength calibration procedure for the Pierre Auger Observatory fluorescence detectors, *Astropart. Phys.* 31 (4) (2009) 305–311. <http://dx.doi.org/10.1016/j.astropartphys.2009.02.009>.
- [10] J. Abraham, P. Abreu, M. Aglietta, et al., The fluorescence detector of the Pierre Auger Observatory, *Nucl. Instrum. Methods Phys. Res. Sect. A: Accel. Spectrom. Detect. Assoc. Equip.* 620 (2010) 227–251, doi:10.1016/j.nima.2010.04.023.
- [11] H. Tokuno, Y. Murano, S. Kawana, Y. Tameda, A. Taketa, D. Ikeda, S. Udo, S. Ogio, M. Fukushima, R. Azuma, M. Fukuda, N. Inoue, K. Kadota, F. Kakimoto, H. Sagawa, N. Sakurai, T. Shibata, M. Takeda, Y. Tsunesada, On site calibration for new fluorescence detectors of the telescope array experiment, *Nucl. Instrum. Methods Phys. Res. Sect. A: Accel. Spectrom. Detect. Assoc. Equip.* 601 (3) (2009) 364–371. <http://dx.doi.org/10.1016/j.nima.2008.12.210>.
- [12] B. Acharya, M. Actis, T. Aghajani, et al., Introducing the CTA concept, *Astropart. Phys.* 43 (0) (2013) 3–18, doi:10.1016/j.astropartphys.2013.01.007.
- [13] J. Aleksy, S. Ansoldi, L. Antonelli, P. Antoran, A. Babic, P. Bangale, M. Barcel, J. Barrio, J.B. Gonzalez, W. Bednarek, E. Bernardini, B. Biasuzzi, A. Biland, M. Bitossi, O. Blanch, S. Bonnefoy, G. Bonnoli, F. Borracci, T. Bretz, E. Carmona, A. Carosi, R. Cecchi, P. Colin, E. Colombo, J. Contreras, D. Corti, J. Cortina, S. Covino, P.D. Vela, F. Dazzi, A. DeAngelis, G.D. Caneva, B.D. Lotto, E. de Oa Wilhelmi, C.D. Mendez, A. Dettlaff, D.D. Prester, D. Dorner, M. Doro, S. Einecke, D. Eisenacher, D. Elsaesser, D. Fidalgo, D. Fink, M. Fonseca, L. Font, K. Frantzen, C. Fruck, D. Galindo, R.G. Lpez, M. Garczarczyk, D.G. Terrats, M. Gaug, G. Ganvitto, N. Godinovi, A.G. Muoz, S. Gozzini, W. Haberer, D. Hadasch, Y. Hababata, M. Hayashida, J. Herrera, D. Hildebrand, J. Hose, D. Hrupec, W. Idec, J. Illa, V. Kadenius, H. Kellermann, M. Knoetig, K. Kodani, Y. Konno, J. Krause, H. Kubo, J. Kushida, A.L. Barbera, D. Lelas, J. Lemus, N. Lewandowska, E. Lindfors, S. Lombardi, F. Longo, M. Lpez, R. Lpez-Coto, A. Lpez-Oramas, A. Lorca, E. Lorenz, I. Lozano, M. Makariev, K. Mallot, G. Maneva, N. Mankuzhiyil, K. Mannheim, L. Maraschi, B. Marcote, M. Mariotti, M. Martinez, D. Mazin, U. Menzel, J. Miranda, R. Mirzoyan, A. Moralejo, P. Munar-Adrover, D. Nakajima, M. Negrello, V. Neustroev, A. Niedzwiecki, K. Nilsson, K. Nishijima, K. Noda, R. Orito, A. Overkemping, S. Paiano, M. Palatiello, D. Paneque, R. Paoletti, J. Paredes, X. Paredes-Fortuny, M. Persic, J. Poutanen, P.P. Moroni, E. Prandini, I. Puljak, R. Reinthal, W. Rhode, M. Rib3, J. Rico, J.R. Garcia, S. Rgamer, T. Saito, K. Saito, K. Satalecka, V. Scalzotto, V. Scapin, C. Schultz, J. Schlammmer, S. Schmidl, T. Schweizer, A. Sillanp, J. Sitarek, I. Snidaric, D. Sobczynska, F. Spanier, A. Stamerra, T. Steinbring, J. Storz, M. Strzys, L. Takalo, H. Takami, F. Tavecchio, L. Tejedor, P. Temnikov, T. Terzi, D. Tescardo, M. Teshima, J. Thaele, O. Tibolla, D. Torres, T. Toyama, A. Treves, P. Vogler, H. Wetteskind, M. Will, R. Zanin, The major upgrade of the {MAGIC} telescopes, part i: the hardware improvements and the commissioning of the system, *Astropart. Phys.* 72 (2016) 61–75. <http://dx.doi.org/10.1016/j.astropartphys.2015.04.004>.
- [14] C. Blaksley, Photodetection Aspects of JEM-EUSO and Studies of the Ultra-High Energy Cosmic Ray Sky, Ph.D. thesis, UNIVERSITE PARIS. DIDEROT (Paris 7), 2013.
- [15] K.K. Hamamatsu Photonics, Stabilized light sources for photomultiplier tubes, 2012. <http://www.hamamatsu.com/resources/pdf/etd/L11416L11494TACC1057E.pdf>.
- [16] Betlux electronics Co, LTD, Round type led lamp bl-l314, 2010. http://www.betlux.com/product/LED_lamp/Super%20Bright%20LED/BL-L314.PDF.
- [17] S. Aiello, D.L. Presti, E. Leonora, N. Randazzo, G.V. Russo, R. Leanza, Aging characterization on large area photo-multipliers, *Nucl. Instrum. Methods Phys. Res. Sect. A: Accel. Spectrom. Detect. Assoc. Equip.* 725 (2013) 151–154. VLVT 11, Erlangen, Germany, 12 - 14 October, 2011 5th International Workshop on Very Large Volume Neutrino Telescopes, The future of high-energy neutrino astronomy.<http://dx.doi.org/10.1016/j.nima.2012.11.130>.